PAPER • OPEN ACCESS

Suspended graphene arrays for gas sensing applications

To cite this article: Rakesh K Gupta *et al* 2021 *2D Mater.* **8** 025006

View the article online for updates and enhancements.

2D Materials

PAPER

Suspended graphene arrays for gas sensing applications

Rakesh K Gupta[1], Faisal H Alqahtani[1,2,*], Omar M Dawood[1,3,*], Marco Carini[4,*], Alejandro Criado[4,*], Maurizio Prato[4,5,6], Suresh K Garlapati[7], Gareth Jones[8], James Sexton[1], Krishna C Persaud[9], Caroline Dang[10,11], Umberto Monteverde[1], Mohamed Missous[1], Robert J Young[1], Stephen Boult[10], Neil Dixon[12], Leszek Majewski[1] and Max A Migliorato[1]

[1] Department of Electrical and Electronic Engineering, University of Manchester, D3a, Sackville Street Building, Manchester M1 3WE, United Kingdom
[2] Department of Physics, Faculty of Science, King Khalid University, Guraiger, Abha 62529, Saudi Arabia
[3] Department of Physics, College of Education for Pure Science, University of Anbar, Anbar, Iraq
[4] Center for Cooperative Research in Biomaterials (CIC biomaGUNE), Basque Research and Technology Alliance (BRTA), Paseo de Miramón 182, 20014 Donostia San Sebastián, Spain
[5] Basque Foundation for Science, Ikerbasque, Bilbao 48013, Spain
[6] Department of Chemical and Pharmaceutical Sciences & INSTM, UdR Trieste, University of Trieste, Via Licio Giorgieri 1, 34127 Trieste, Italy
[7] Department of Materials, University of Manchester, Mills Building, Manchester, United Kingdom
[8] Center for Innovation (UMI3), University of Manchester, Grafton Street, Manchester M13 9XX, United Kingdom
[9] Department of Chemical Engineering and Analytical Science, School of Materials, University of Manchester, Manchester, United Kingdom
[10] Department of Earth and Environmental Science, The University of Manchester, Manchester, United Kingdom
[11] Nasa Ames Research Centre, Moffet Field, CA, United States of America
[12] Manchester Institute of Biotechnology, University of Manchester, Manchester, United Kingdom
* These authors contributed equally.

E-mail: rakesh.kumar@manchester.ac.uk and rkguptt@gmail.com

Abstract

Suspended graphene (SUS-G) has long been hailed as a potential 'true graphene' as its conductive properties are much closer to those of theoretical graphene. However, substantial issues with yield during any device fabrication process have severely limited its use to date. We report the successful fabrication of a fully operational prototype of a miniature 9 mm^2 suspended graphene array sensor chip, incorporating 64 graphene sensor devices, each comprising of 180 SUS-G membranes with ever reported 56% fully intact graphene membranes for sensitive and selective gas sensing applications. While a bare sensor chip can operate as a sensitive gas sensor for a variety of gasses such as ammonia, nitrogen dioxide and carbon monoxide, down to ppm/ppb concentrations, a tetrafluorohydroquinone functionalized sensor acquires specificity to formaldehyde gas molecules with limited cross-sensitivity for ethanol, toluene and humidity. Unlike an equivalent device with fully supported functionalized graphene sensor, a functionalized SUS-G sensor can be furthermore reset to its baseline by using UV assisted desorption instead of substrate heating. The low power UV irradiation does not show severe damage to the SUS-G structures and loss of functional probes for the formaldehyde gas—a previously unreported feature. A resettable and selective formaldehyde gas sensor array with mass manufacturability, low power consumption and overall dimensions down to 1 mm^2, would represent a significant technological step forward in the development of an electronic nose, for the simultaneous detection of multiple-target gases, with potential for integration in portable electronic devices and the internet of things.

1. Introduction

Air pollution is the largest environmental contributor to ill health and responsible for growing mortality rate at an alarming pace. The World Health Organization (WHO) reported that indoor air pollution, produced from an inefficient use of solid fuels and kerosene for cooking, was responsible for close to 4 million premature deaths in 2016, which is 7.7% of the global mortality. Ambient air pollutants consist of gases such as nitrogen dioxide (NO_2), sulphur dioxide (SO_2), methane (CH_4), ammonia (NH_3), carbon dioxide (CO_2) and carbon monoxide (CO). As these gasses play a major role in causing ill health, their identification in the environment demands an accurate and continuous air quality monitoring (AQM), especially in large urban areas. The real-time high resolution AQM requires deploying sensitive, selective and cost-effective low-power and wide-area network of miniaturized gas sensors in high pollution zones. Currently, the performance standards in solid state gas sensors are benchmarked by MOX technologies, although these have known limitation of their lifetime performance [1–7]. Many advanced materials including carbon nanomaterials have been proposed as a replacement for MO_x platforms [8–13]. Recently, monolayer graphene has shown potential for sensitive bio-, chemical, and strain sensors, because of its properties e.g. scattering free charge transport over several micro-meter length scales [14–19], and high binding affinity to a variety of bio and gas molecules [20, 21].

Gas sensors based on graphene, connected as a resistive, Hall effect or in the field-effect transistor (FET) configuration, as single device exhibit extrapolated detection limits down to parts per billion (ppb), trillion (ppt) or even single molecule have been observed [22–24]. There are three main barriers to market adoption: firstly, the intrinsic properties of pristine graphene are severely affected by its interaction with the host substrate particularly charge trapping (or contamination) due to the conventional wet chemical transfer [25, 26]. Secondly, industrial wafer-scale fabrication is size limited when using wet chemical transfer of chemical vapour deposition (CVD) graphene [27–29]. Thirdly, a generic sensor is useful but to have a viable marketable technology, it is essential to attain specificity to a single useful gas obtained either by sensor surface modification or sophisticated machine learning [30–34]. A potential solution to these challenges is the use of freestanding or suspended graphene (SUS-G) sheet(s) [35–37]. Removal of the Van der Waals interaction between graphene and the surface atoms of the substrate leads to improved mechanical, electronic and chemical properties compared to substrate supported graphene (SUP-G) [35, 38], e.g. electron mobility has been reported to increase up to $\sim$200 000 cm^2 V^{-1} s^{-1}

(from 2000 to 20 000 cm^2 V^{-1} s^{-1} for SUP-G) and gas detection sensitivity increased to single molecule level [22].

In this work, we report a scalable approach to the fabrication of suspended graphene array-based sensors (SGAS) [39], where unfunctionalized SGAS chips shows a high sensitivity for common air pollutants (NO_2, NH_3 and CO) but a functionalized SGAS shows specificity to formaldehyde (with no cross-sensitivity for ethanol, toluene and humidity) and recoverable using low power UV (390 nm, $\sim$200 mW at 6.5 V for $\sim$5 min) irradiation.

2. Results and discussion

2.1. SGAS chip layout and characterization

Monolayer CVD graphene is generally polycrystalline, very often with grain size of only a few tens of microns. In practice, the proposition of using SUS-G films to overcome substrate effects which limit its conductivity, appears at odds with the requirements of current volume manufacturing of solid-state sensors [40]. In fact, inherent defects at the grain boundaries result in tearing of the suspended film whilst undergoing simple lithographic steps like supporting polymer removal or lift-off steps [40, 41]. This generally results in a poor yield of SUS-G membranes (especially with monolayer graphene) and batch-to-batch variations in the electrical properties of the devices.

To overcome these issues, we used a novel strategy, i.e. to create square/circular (tens of micron sized areas/diameter) SUS-G membranes, configured as an array, with micron sized separation (pitch) between them. This results in areas of SUS-G alternating with areas of SUP-G, but with the potential for much better manufacturability. The challenge is to find the ideal trade-off between maximizing the conductive/sensing properties of graphene (by increasing the ratio of suspended to SUP-G) and maintaining a high yield (by finding the shape (square/circular) and largest size membranes array) of the membranes array that can remain intact during the entire micro fabrication process. This is very different from previously reported large graphene membranes obtained on metal (Cu) substrate or obtained by graphene/polymer stack transfer on drums, but without top metal contacts formation, as these devices cannot be used for gas sensing applications [36, 42].

We thus fabricated a full-scale (15 mm × 15 mm) die (figure 1(a) (top left)), containing 16 miniaturized (9 mm^2) individual sensor chips (figure 1(a) (top right)), each containing 64 individual sensors. As these individual sensors are connected in parallel, the architecture is tolerant to imperfection of some of the sensors by performing an analog average of the output signal between them. Each individual
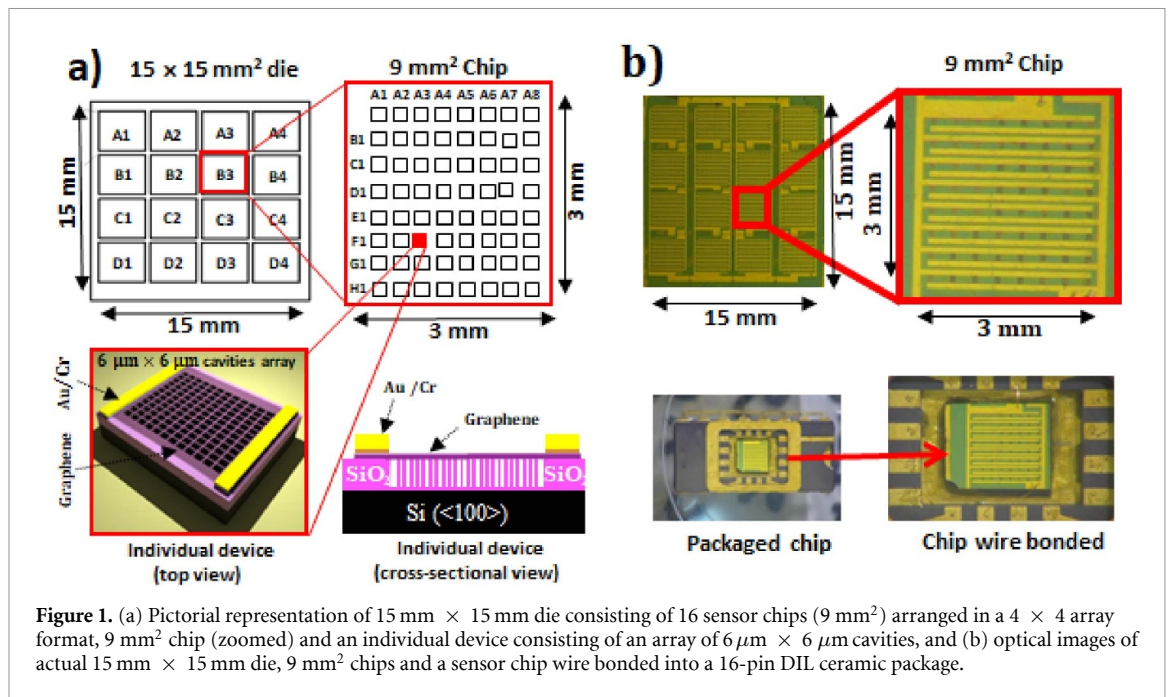
Figure 1. (a) Pictorial representation of 15 mm × 15 mm die consisting of 16 sensor chips (9 mm²) arranged in a 4 × 4 array format, 9 mm² chip (zoomed) and an individual device consisting of an array of 6 µm × 6 µm cavities, and (b) optical images of actual 15 mm × 15 mm die, 9 mm² chips and a sensor chip wire bonded into a 16-pin DIL ceramic package.

sensor (figure 1(a) (bottom)) consists of a mono-layer graphene, suspended over an array of 180 cavities, which further guarantees tolerance against some of the membranes being broken during the fabrication process. While each device occupies an area of 120 µm × 100 µm, two different types of devices were fabricated with square (6 µm × 6 µm) and circular (6 µm diameter) membranes. After many attempts, this was found to be an upper limit, having carefully balanced the largest size with the constraint of high yield, which was found to drop off significantly for sizes larger than 6 µm × 6 µm (square) and 6 µm diameter (circular) membranes. The ideal pitch (2 µm) was determined by the resolution of UV lithography system, while the depth ∼1 µm was identified as the minimum depth that avoids the SUS-G touching the bottom of the cavity while bowing under e.g. pressure differences on either side of the membrane. This was primarily driven by our previous work on back gated mechanical fluctuation SUS-G structures [43]. The graphene layer is clamped on two opposite sides by Cr (10 nm)/Au (100 nm) contact lines (figure 1(a) (bottom)), to ensure the best possible Ohmic contact (as opposed to simply laying the graphene on top of the metal contacts) [40]. Figure 1(b) shows the optical images of the die (top left), sensor chip (top right) and chip wire-bonded in a 16-pin dual-in-line (DIL) ceramic IC package case (bottom).

As an example, scanning electron microscope (SEM) images (figures 2(a) and (b)), obtained from a chip having square graphene membranes, confirm the presence of fully covered (green box), partially covered (red box), and some ruptured (yellow arrow) membranes. The cavities covered with graphene, being electrically conductive, appear dark

in SEM images and whilst open cavities (no graphene) appear bright due to charging of the oxide surface (also see figure S2, SI (available online at stacks.iop.org/2DM/8/025006/mmedia)). The ring-shaped features that appeared at the bottom of cavities in oxide film (SiO_2) were produced during the reactive ion etching (RIE) of SiO_2. Graphene membranes appear to rupture at the grain boundaries due to low bond strength [44]. Most of the cavities on the SiO_2 surface are covered by the graphene sheet as revealed by a 30 m × 30 m topography atomic force microscope (AFM) micrograph shown in figure 2(c). A line profile graph for three distinct lines, line 1 (black), line 2 (red) and line 3 (blue) drawn on the topographic AFM image (figure 2(c)), clearly indicates fully suspended and partially broken cavities. The monolayer graphene sheet tends to sag into the cavities, which potentially can touch the bottom surface for larger cavities [43, 45, 46]. However, the resilience of the aluminium/positive photoresist/graphene (Al/PPR/Gr) graphene film stack (GFS) (sections S1, SI), employed in this study, restrains this sagging, which is evident from the line profile plots. The cavity depth is ∼1 µm (figure 2(c)), (line 2 (red)) and it appears recessed by ∼150 nm (line 1 (black)) into the cavity where graphene is mostly suspended over the cavities, which means it is suspended over the cavity at a height of ∼835 ± 20 nm. SEM images of chips from different batches were collected and analysed for estimating the circular/square graphene membrane yield. The circular membranes show an average ∼56% intact, ∼30% partially suspended/ruptured and ∼14% broken membranes (figure S3.1 and table S3.1, SI) when calculated from three samples, each having 180 circular cavities. Similarly, an average of ∼15% intact, ∼80% ruptured and ∼5% broken
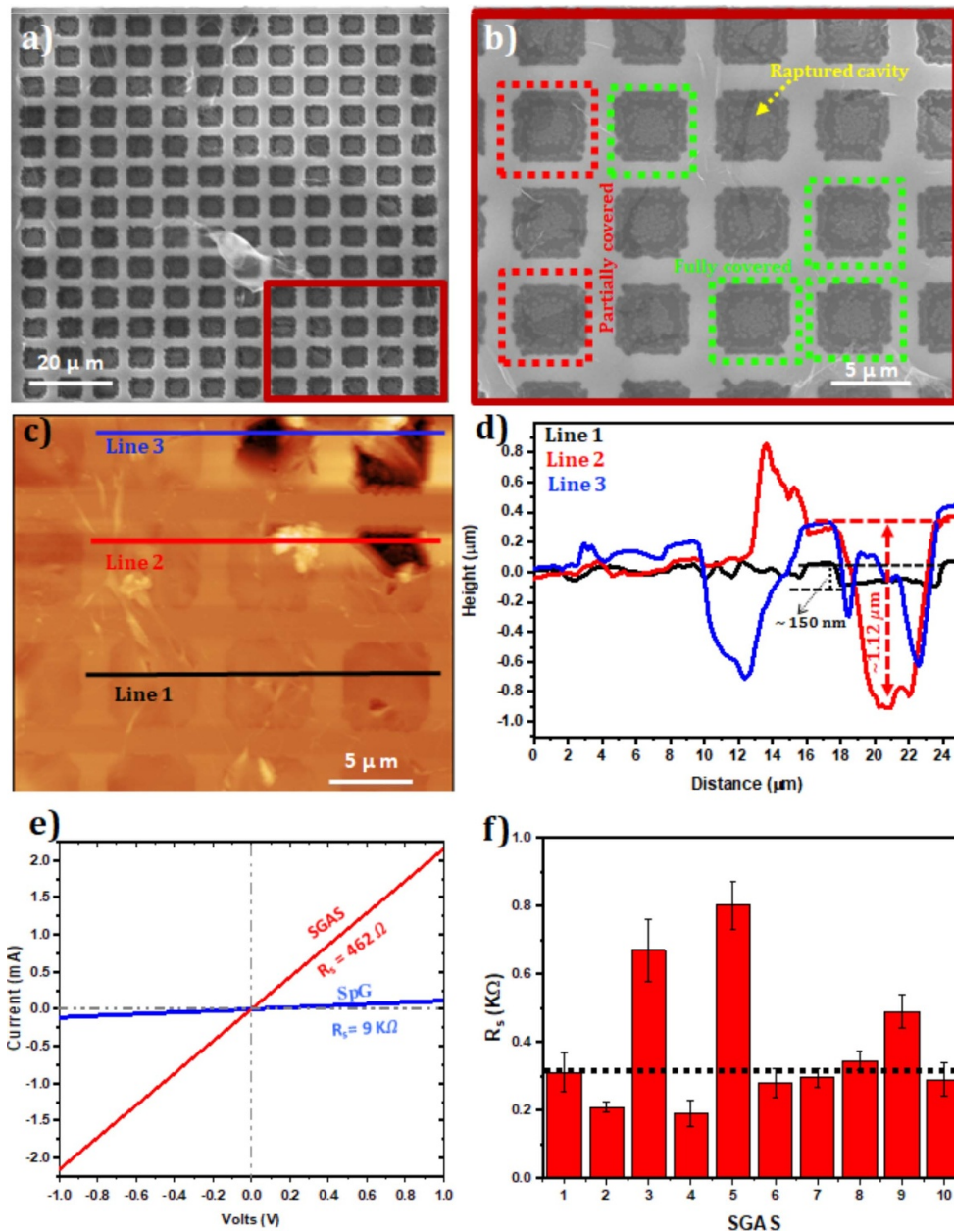
Figure 2. (a) SEM image of square cavities covered with graphene film; (b) highlight region (red solid box) in (a) showing fully covered (green dotted box), partially covered (red dotted box) and ruptured (yellow dotted arrow), (c) AFM micrographs of a 900 μm^2 height image of cavities array, (d) line profile graph for three lines (line 1 (black), line 2 (red) and line 3 (blue)) drawn on height image in (c), (e) selective typical current–voltage (*I–V*) plots for SGAS chip (red) and supported graphene (SpG) (chip having similar device architecture and device dimensions but graphene film is fully supported (no cavities) on SiO_2/Si substrate) chip (blue) and (f) statistical total resistance 'R_s' measurement (parallel equivalent of 64 devices plus contact resistance) for SGAS. (It should be noted that R_S data shown in (f)) was collected from ten batches of a 15 mm × 15 mm dies and plotted as rectangular bar plot representing an average 'R_s' (1/Slope of *I–V* plot) of 3–5 sensor chips (error bars represents the standard deviation from each batch).

square graphene membranes yield can be suggestive (roughly observed from figures S2 and S3.2, SI), which is evidently less than that for the circular membranes. A potential reason for the large percentage of ruptured membranes of square membranes is likely due to the non-uniform strain on graphene around the sharp edges that results in tearing of graphene on most of the square cavities [43]. Topographical data shown in figures 2(a)–(d) qualitatively confirms the usefulness of the combined use of GFS based graphene transfer and critical point drying (CPD)

cleaning methods, presented in this work, to achieve a high yield of SUS-G membrane structures surviving the complete fabrication process. This yield is e.g. 20 times larger than the 2.7% value reported by Wagner *et al* [40]. As the graphene used in this work only had a ~10 μm grain size, it can be anticipated that the yield of fully covered cavities would improve even more should larger grain-size CVD graphene become available.

To evaluate the quality of graphene surface obtained post-fabrication, Raman mapping were also

performed for both the SUP-G and SUS-G regions within a square/circular cavity. Section 4 in SI provides a detailed discussion of Raman spectrum data analysis, which confirms the high quality of SUS-G regions in comparison with SUP-G for both the square/circular membrane configurations. Here, if we only focus on intensity ratio (I_{2D}/I_G), which is reported as inversely proportional to the number of graphene layers and proportional to the uniformity of the layer [47]. The I_{2D}/I_G values varies from 1.7 to 2 for SUS-G, 0.3 to 0.7 for SUP-G for a pair of square membranes (figure S4.1(e)) and much improved for circular membranes (figure S4.3(g)). One conclusion, thus, can be drawn that SGAS with circular membranes, containing ∼56% of SUS-G, is significantly less doped by the hydroxyl (–OH) and silanol groups (Si–O–H) on the substrate surface, which are well-known sources of p-doping in graphene [25, 48].

Lastly, we compare the total equivalent resistance (R_S) of two chips, which is identical in all aspects but for the presence/absence of cavities (SGAS and SUP-G sensor (SpG) chips) in the sensor substrate. For both these chips, R_S is obviously a parallel equivalent resistance of 64 devices (plus the contact resistance). It is evident from figure 2(e) that the resistance shown by SGAS (462 Ω) is an order of magnitude lower than that of an SpG chip (∼9 kΩ). This is of particular importance as lower sensor resistance can potentially increase the ability to detect small electrical signals across the load resistor R_L used in the detection circuit, potentially resulting in lower limit of detection (LOD). Additionally, an array of mostly intact graphene membranes within sensor devices connected in parallel can enhance the signal to noise (S/N) ratio and sensitivity due to the broadening of the active area for reaction [49]. One issue that still needs resolving is that R_S for both types of chips, shows variations from batch to batch, although, it is worse for SpG sensor (large error bars in figures 2(f) and S3.2 (SI)). It is, however, anticipated that this would also improve significantly with a large grain-sized crystalline CVD graphene.

Finally, it is apparent that while mobility of SUS-G is expected to be 10^3 higher than that of SUP-G [35], this is not translated directly to a reduction of the total chip resistance. This is because firstly, in a 120 μm × 100 μm graphene channel, 46% of SUP-G area (pitch) contribution is significant in comparison with even for a 100% yield of SUS-G (all 180 membranes intact) area, and secondly the total resistance measured is not just the resistance of the graphene channel, but the R_S of the chip, which includes the metal contacts. However, even a single order of magnitude reduction in the total resistance of the chip demonstrates the significant performance advantages of using SUS-G.
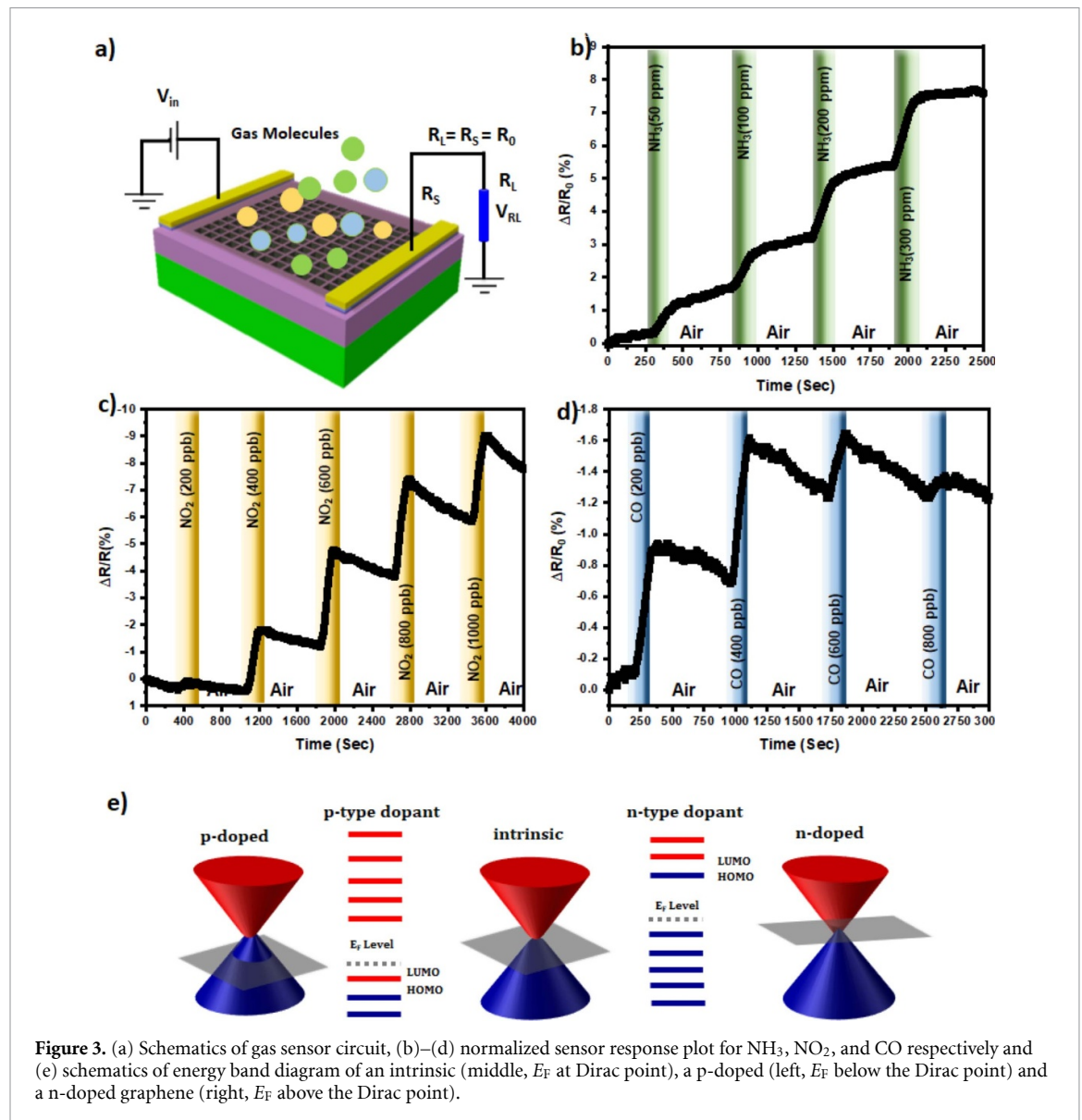
SGAS with 56% reproducible yield of circular membranes in comparison with low yielded (∼15%) square graphene membranes is expected to perform better, especially for sensing applications. The high quality (low p/n-doping) of SUS-G structures and low resistance of connected devices on an SGAS chip could benefit as miniaturized gas sensing. In the following section, we present the use of circular membrane based pristine SGAS as a non-specific and a functionalized SGAS as selective gas sensor for the detection of different environmental gases.

2.2. Gas sensing

2.2.1. Pristine SGAS for NH₃, NO₂ and CO detection

A recent study conducted by Buckley *et al* suggests the enormous potential of 2D material-based gas sensors for environmental monitoring [14]. To assess the potential of SGAS as a gas sensor for AQM, we tested the detection and quantification of common environmental pollutant gases (NO_2 and CO) and agricultural product life cycle/livestock health markers (NH_3) using circular membrane based bare SGAS (chemically unmodified graphene) chip. Figure 3(a) shows the equivalent circuit diagram of the sensor chip: any change in R_S due to the adsorption of different gas molecules at the graphene surface is identified by measuring the change in voltage signal (V_{RL}) across a load resistor R_L connected in series with R_S (figure 3(a)), where $R_L = R_S = R_0$ (R_0 is the initial value (or base line) of sensor resistance). The sensor chip was exposed to increasing concentrations of gas (NH_3, NO_2 or CO), with cycles consisting of 120 s exposure at a fixed concentration (at room temperature (RT) and atmospheric pressure), followed by a ∼600 s clean air exposure for recovery, and the total mass flow was maintained constant during exposure and recovery cycles. Gas concentrations were controlled by a mass flow controller (section S5, SI) used to mix appropriate amount of respective gas with compressed air. In this study, different batches of chips were used for different gases to completely eliminate the risk of cross contamination. Figures 3(b)–(d) show the normalized sensor response ($\Delta R/R_0$) × 100%, where, $\Delta R = R_S - R_0$ and the change in R_S with respect to gas concentrations is extracted from equation $R_S = R_L (V_{in}/V_{RL} - 1)$ (figure 3(a)) for NH_3, NO_2 and CO gases respectively. An increase/decrease in graphene conductivity (hole-conductivity or electron-conductivity) depends upon the initial doping state of graphene and types of dopants adsorbing on its surface, which can be understood from the energy band diagram shown in figure 3(e). For example, n-doping gases (e.g. NH_3, CO) decrease the hole-conductivity of a p-doped graphene (Fermi level (E_F) below Dirac point, figure 3(e) (left)) but increases the electron conductivity of a n-doped graphene (E_F above the Dirac point, figure 3(e) (right) [50, 51]. On the other hand, a hole doping gas (e.g. NO_2) increases the hole-conductivity of

Figure 3. (a) Schematics of gas sensor circuit, (b)–(d) normalized sensor response plot for NH_3, NO_2, and CO respectively and (e) schematics of energy band diagram of an intrinsic (middle, E_F at Dirac point), a p-doped (left, E_F below the Dirac point) and a n-doped graphene (right, E_F above the Dirac point).

a p-doped graphene (E_F below the Dirac point, figure 3(e) (left)) but decreases the electron conductivity of n-doped graphene (E_F above the Dirac point, figure 3(e) (right)). Therefore, the detection sensitivity for any gas can be tuned whilst shifting E_F above or below the Dirac point (charge neutrality point or intrinsic level, figure 3(e) (middle)) [23, 52]. While pristine graphene gas sensors are non-specific and cannot discriminate between the analytes, they can, however, identify whether a gas acts as an electro donor or acceptor. Here, an increase/decrease in conductivity (hole/electron) of SGAS chip, due to the adsorption of gases, is presented as decrease/increase in $\Delta R/R_0$ (or R_s).

For example, with the increasing concentration of NH_3 and NO_2, $\Delta R/R_0$ increases and decreases (or R_S increases and decreases) respectively (figures 3(b) and (c)), because the analytes are strong reducing/oxidizing agents and donate/accept electrons upon interaction with the graphene

(p-doped) surface thus increasing/decreasing the $\Delta R/R_0$ [24, 51]. The responses to NH_3 and NO_2 show sensitivity of the sensor for these two gases, which while being previously reported for micron sized areas of mechanically exfoliated graphene [51, 53], is here proven in a fully scaled graphene chip.

It should also be noted that an SUP-G device exposed to CO, a reducing gas (n-dopant), has a positive relationship between concentration and sensor resistance [54], whereas, the SGAS showed a negative relationship between concentration and $\Delta R/R_0$ (figure 3(d)) on exposure to CO, as it does for oxidising NO_2 gas. CO, as an electron donating gas, can increase the conductivity of graphene only if the E_F is either near or above the Dirac point, which is similar to what Chen *et al* [23] reported for NH_3. While a low-doping is possible in SUS-G regions of SGAS (Raman mapping data discussed in section S4, SI), a slight n-doping could be from Cr/Au metal contacts deposition (Cr/Au has higher work functions

than graphene) [23, 55]. Thus, an electron doping from CO gas into a slightly n-doped graphene causes an increase in the electron-conductivity (figure 3(e) (right)) leading to a negative relationship between concentration and $\Delta R/R_0$ (figure 3(d)). The SGAS responsivity is strikingly higher (with a pronounced saturation at higher concentrations) than the one reported with an SUP-G device [54]. The increased responsivity and saturation at higher concentration could be due to the up-shifting of E_F (n-doped graphene E_F), which might not be favourable for higher concentration of CO gas to further increase the electron conductivity at ambient conditions. The actual reason behind the early saturation of CO sensor (for CO [>400 ppb]) needs further studies through specific modelling of CO molecules interaction with graphene surface under doped/undoped conditions.

It is also noted that none of the gas exposures depicted in figure 3 show a complete recovery at RT, however, a very slowly gas desorption is apparent for NO_2 (~1 h for 200 ppb) and NH_3 (>12 min for 300 ppm) as the chamber is purged with compressed air (see figure S5.2, SI). The desorption rate (or recovery time) has been reported to be significantly enhanced by substrate heating of an SUP-G based sensor and, moreover, a micro heater can be easily fabricated on the chip to enhance the desorption by Joule heating [49, 56]. An attempt to desorb the gas molecules by heating SGAS chip at 150 °C on a hot plate (as used by Schedin *et al* [24] for desorption of gas) resulted in an increase in its R_S (tens of kΩ, a values same as of an SpG sensor). A change in R_s upon substrate heating is expected due to the better graphene-substrate adhesion (annealing induced doping effects) and the irreversible physical straining and/or rupture of the graphene membranes, caused by hot air inside the cavities exerting pressure difference on the graphene sheet (See figure S5.3, SI) [57, 58]. Therefore, direct substrate heating to speed the recovery (gas desorption) is not recommended for SGAS. Alternatively, low energy ultra-violet (UV at 390 nm) assisted gas desorption, without damaging the SUS-G structure, is discussed later. SGAS sensor's sensitivity (response/conc.), LOD, rise time and recovery time for different gases were calculated from the data in figure S5.4 (SI) and a performance comparison with previous work is given in table 1. The LOD was estimated to be lower for NO_2 (~108 ppb) and CO (~50 ppb) compared to NH_3 (~34 ppm). Compared to the use of SUP-G, SGAS shows responsivity for NO_2 which is two orders of magnitude better than other reports [23, 51], for NH_3 close to the previously reported values [23, 51, 59], and for CO higher (~0.8% for 400 ppb, 2×10^{-3} S [ppb]$^{-1}$) than the one reported for an SUP-G device (~3.27% for 100 ppm, 3.2×10^{-5} S [ppb]$^{-1}$) [54]. The signal, however, saturates at higher concentration (>600 ppb) for CO. Here, we showed the sensitivity of

SGAS to various gases of interest, this sensor would produce an aggregate signal if exposed to an environment containing a mixture of gases. SGAS as a selective gas sensor is described in the following section.

2.2.2. Functionalized SGAS for selective formaldehyde (HCHO) sensor, sensor recovery and specificity

The selective detection of HCHO has been demonstrated by non-covalent functionalization of CVD graphene surface with 2,3,5,6-tetrafluorohydroquinone (TFQ) on an SiO_2/Si substrate [62]. To the best of our knowledge, a similar attempt of specificity has not been made with an SUS-G membrane device as presented in this study. SGAS chip with circular membranes was non-covalently functionalized with TFQ, and to determine the effectiveness of the functionalization process; SEM, x-ray photoelectron spectroscopy (XPS) and Raman mapping analysis were performed. Firstly, the structural integrity of the SUS-G film (intact membrane) before/after the chemical modification was investigated by SEM. It is confirmed (figures S5.5(a) and (b) (SI)) that the immersion method, employed for the chemical modification, does not cause collapsing of membranes post TFQ treatment. Secondly, the quality of the TFQ coating was investigated by comparison of XPS data obtained before and after the coating (figures 4(a) and (b)). This clearly shows F1s signal absorbance between the binding energy of 650 eV to 750 eV (inset; figure 4(b)), which confirms the presence of fluorine atoms (fluorine (F, 1.4%), carbon (C, 62.0%), oxygen (O, 35.9%) and iodine (I, 0.7%) atoms) at the sensor surface compared to the signal for a pristine graphene (inset; figure 4(a)). The small iodine peak could be due to Au etchant (section S1b, SI) residual contamination on this particular chip. It should be noted that the total effective graphene area is ~1 mm² (12 000 μm² graphene/sensor, 64 sensors/SGAS chip) whereas the XPS system has 3 mm spot size and, therefore, collected an average absorbance spectrum of the entire SGAS chip surface. Hence, only a weak F1s absorbance signal was obtained for the π–π bonding and/or hydrophilic interactions of TFQ molecules with graphene surface.

The Raman spectrum can also provide additional information concerning the chemical modification of graphene [65], e.g. for a non-covalent modification of graphene, the shift of the G-peak/2D-peak position is highly sensitive to the doping of the graphene structure [66, 67]. Ji Eun Lee *et al* and Yapin Dan *et al* reported that the effects of low level doping on graphene are more pronounced for the G-peak position than the 2D-peak position because of the non-adiabatic electron–phonon coupling [68, 69]. However, Bo Tang *et al* reported the sensitivities of 2D-peak for high p-doping [70]. To further evaluate the chemical modification of SUS-G membranes in SGAS, optical micrographs and Raman mapping (30 data points), using a WITek

Table 1. Performance comparison of SGAS with work reported in literature.

Graphene material	Transduction mechanism	Target gas (s)	Sensitivity	LOD	Rise time	Recovery time	Ref.
Porous-G	FET	NO_2	$0.0432\ (\Delta R/R_0)$/ppm	15 ppb	5–7 min	10 min	[60]
		NH_3	$0.0071\ (\Delta R/R_0)$/ppm	160 ppb			
CVD-G (Non-suspended graphene)	Resistive	NO	$2.51 \times 10^{-3}\ (\Delta G/G_0)$/ppm	158 ppt	Few min	10 min	[23]
		NO_2	1.29×10^{-4} "	2.06 ppt			
		NH_3	9.95×10^{-6} "	33.2 ppt			
		CO_2	2.75×10^{-6} "	136 ppt			
		H_2O	3.14×10^{-6} "	103 ppt			
	Resistive	NO_2	$9.7 \times 10^{-6}\ \text{ppm}^{-1}$	100 ppb	Few min	100 min	[61]
		NH_3		500 ppb			
	Resistive/ Capacitive	CO_2	$9.7 \times 10^{-6}\ \text{ppm}^{-1}$	100 ppb	3 s	30 min	[51]
	Resistive	NH_3	$0.049\ (\Delta R/R_0)$ at 8.8 sccm	—	—	70 s	[49]
	Resistive	HCHO	$10\%\ (\Delta R/R_0)$ at 1.5 ppm	—	30.83 for 1.5 ppm	—	[62]
ME-PG	Hall geometry	NO_2	$\Delta R > 2.5\ \Omega$/electron	Single molecule	6 s	—	[24]
	Resistive	Ethanol Toluene	$-50\ (\Delta R/R_0)$/ppm	—	—	—	[33]
	Resistive	CO_2	$\Delta R = {\sim}60\ \Omega$/electron	Single molecule	—	—	[22]
	Resistive	Ethanol Methanol IPA	—	—	3 min	10 min	[63]
Epi-G	Resistive	NO_2	0.025–$0.1\ (\Delta G/G_0)$	—	5 min	—	[64]
SGAS*	Resistive	NH_3	$+0.02803\ \Delta R/R_0$/ppm	${\sim}34$ ppm	${\sim}180 \pm 5$ (s)	${\sim}12$ min (UA)	This work
		NO_2	$-0.01273\ \Delta R/R_0$/ppb	${\sim}50$ ppb	${\sim}130 \pm 4$ (s)	${\sim}90$ min (UA)	
		CO	$-0.00858\ \Delta R/R_0$/ppb	${\sim}108$ ppb	${\sim}100 \pm 2$ (s)	—	
		HCHO	$-0.01056\ \Delta R/R_0$/ppm	—	${\sim}4 \pm 0.87$ (min)	${\sim}5 \pm 0.9$ (min) (UV assisted)	

G, graphene; ME-PG, mechanically exfoliated pristine graphene; CVD, chemical vapor deposition; rGO, reduced graphene oxide; Epi-G, epitaxial graphene; SGAS, suspended graphene array-based sensor; UA, unaided; ppm, parts per million; ppb, parts per billion; ppt, part per trillion; sccm, square cubic centimetre; s, second; min, minute; $\Delta R/R_0$/ppm, resistive sensitivity; $\Delta G/G_0$/ppm, conductive sensitivity; and UV, ultra violet exposure.
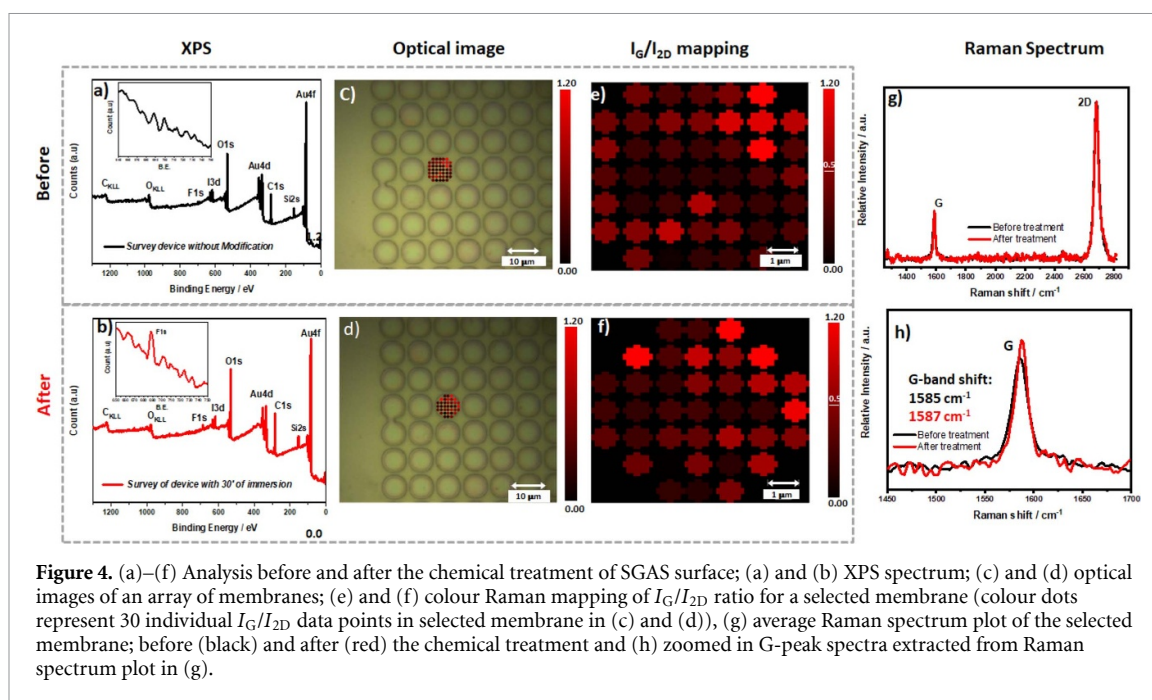
Figure 4. (a)–(f) Analysis before and after the chemical treatment of SGAS surface; (a) and (b) XPS spectrum; (c) and (d) optical images of an array of membranes; (e) and (f) colour Raman mapping of I_G/I_{2D} ratio for a selected membrane (colour dots represent 30 individual I_G/I_{2D} data points in selected membrane in (c) and (d)), (g) average Raman spectrum plot of the selected membrane; before (black) and after (red) the chemical treatment and (h) zoomed in G-peak spectra extracted from Raman spectrum plot in (g).

alpha 300 R Raman microscope, were produced for individual graphene membranes before (figure 4(c)) and after (figure 4(d)) the chemical modification with TFQ. The I_G/I_{2D} ratio colour map data representing the quality of graphene membrane before (figure 4(e)) and after (figure 4(f)) the chemical treatment confirms the modification in SUS-G post TFQ coating.

A careful examination of the average Raman spectrum of the selected membrane (figures 4(g) and (h)) suggests that after TFQ modification there is no D-peak intensity increase but a small up-shift (blue shift) of $\sim$2 cm^{-1} in G-peak (figure 4(h)), no significant shift for 2D-peak position, and small sharpening of G/2D-peaks indicating low doping and less defect/traps. This concurs with results obtained by Tang *et al* [62], confirming that TFQ functionalization induces a small amount of doping but no defects (increase in D-peak intensities) because the TFQ molecules are non-covalently connected with graphene by π–π bonds or hydrophilic interactions. A statistical data analysis performed over 4000 data points on several suspended membranes (figure S5.6, SI) further supports the above claims. In order to confirm the doping of graphene, the average values of G-peak and 2D-peak of the graphene component 3 (figure S5.6) was compared before and after TFQ modification. Average G-peak, before (1589.2 $\pm$ 0.66 cm^{-1}) and after (1583.6 $\pm$ 0.16 cm^{-1}), positions indicate a down shift of $\sim$5.6 cm^{-1} whereas the average 2D-peak, before (2684.8 $\pm$ 0.36 cm^{-1}) and after (2684.5 $\pm$ 0.20 cm^{-1}), positions indicate a down shift of $\sim$0.4 cm^{-1}. While a small down shift (red shift) in 2D peak indicates small doping, however, the recorded $\sim$5.6 cm^{-1} average red shift (down shift)

of G peak could be attributed to the increased strain effect and electron doping after TFQ modification [68, 71]. These results were further validated by TFQ modification of a fully SUP-G on SiO$_2$ substrate, which clearly shows the difference in doping effect in TFQ functionalized suspended and SUP-G. The Raman data analysis for an SUP-G (figure S5.7, SI) reproduces the results as obtained by Tang *et al* [62].

2.2.2.1. Selective HCHO detection, sensor recovery and specificity

HCHO is one of the causes of what is called the 'sick building syndrome' in huge skyscrapers, giving people headache, nausea, eye irritation and affect respiratory organs. HCHO is an indoor air pollutant besides CO$_2$, CO, NO$_2$, CH$_4$, NO, etc. The permissible exposure limit for HCHO in the workplace is 0.75 ppm measured as an 8 h time-weighted average (TWA). A short-term exposure, permissive exposure limit is 2 ppm maximum allowed for 15 min period [72]. The action level—which is the standard's trigger for increased industrial hygiene monitoring and initiation of worker medical surveillance—is 0.5 ppm when calculated as an 8 h TWA and throat and nasal irritation can occur at levels of 0.08 ppm [72, 73]. Whilst carbon nanotubes (CNTs) based array sensor has shown detection limit for HCHO concentration down to 10 ppb [73], a micrometre sized SUP-G device, functioned with TFQ molecules, was able to detect 1.5 ppm of HCHO [62]. In this work, we only aim to demonstrate the feasibility of functionalizing SGAS, e.g. with TFQ molecules as HCHO receptors, using wet chemical treatment methods presented herewith, and cross-sensitivity for ethanol toluene and humidity, rather than achieving a LOD-meeting the permissible exposure limits.
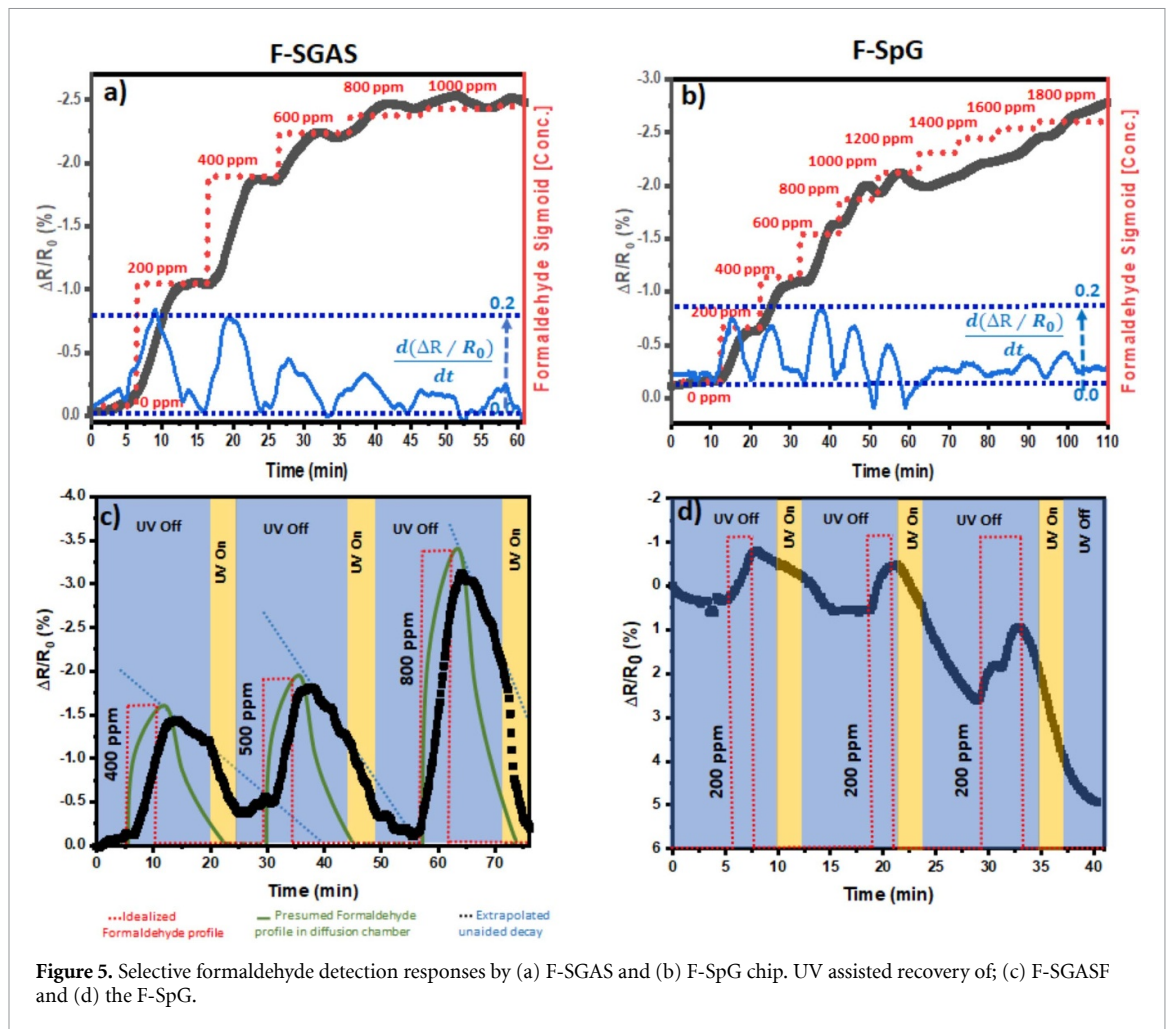
Figure 5. Selective formaldehyde detection responses by (a) F-SGAS and (b) F-SpG chip. UV assisted recovery of; (c) F-SGASF and (d) the F-SpG.

It is important to note that with a large volume (5 l) (figure S5.1(c), SI), of the adapted gas chamber, a diffusion flow mechanism for higher concentration (0 ppm to 1000 ppm) of HCHO was achievable for sensing demonstrations. Tests of the ability to selectively detect HCHO were carried out on a functionalized SGAS (F-SGAS) chip and similarly functionalized SpG (F-SpG) chip. Modified sensor chips (F-SGAS/F-SpG) were tested for the HCHO specificity against two control gases (ethanol and toluene) and humidity. Prior to switching on the power (DC, 1 V) to the sensor, the gas chamber was flushed with compressed air and sealed. F-SGAS/F-SpG graphene chips were electrically stabilized for slightly more than 10 min after being powered on (data not shown) and prior to exposure to HCHO or control gases in the gas chamber. The chamber was not evacuated during the gas injections and consequently it would not result in immediate changes in gas concentration at the sensor, but for the purposes of this study this discrepancy is negligible. Tang *et al* suggested adsorption of HCHO molecules at graphene surface occurs whilst forming weak and reversible intermediate products due to the interaction of HCHO with OH groups of TFQ [62]. These intermediate products thus transfer electrons

into the graphene resulting change in sensor resistance. It is noted that not much literature is available for a clear understanding of a positive (or negative) change in resistance that could occur due to adsorption of HCHO at TFQ grafted CVD graphene. For example, in case of F-SGAS/F-SpG, the sensor shows a negative change in resistance with an increase in HCHO concentration (figure 5), contrary to what reported earlier by Tang *et al* for an SUP-G sensor [62]. Where the n-doping of F-SGAS is supported by the Raman data analyses (red shift in G/2D peaks, figures S5.6 and S5.7), the decrease in sensor resistance is similar to the interaction of electron donating CO gas with SGAS (figure 3(d), though nonfunctionalized). The possible mechanisms for this negative change (or decrease) in resistance could be (a) the transfer of electron from HCHO molecules into an intrinsic or slightly n-doped graphene (E_F near or above the Dirac point, figure 3(e), right) and/or (b) the presence of induced dipoles on the graphene due to the adsorption of the formaldehyde causing increase in conductivity of graphene. The F-SGAS chip (figure 5(a)) is more sensitive than the F-SpG (figure 5(b)). This is illustrated by comparing the first derivates of respective sensor's response (blue lines in figures 5(a) and (b)), giving

an idea of the kinetics of the sensors response, which for the F-SGAS device are a series of regularly spaced peaks that decrease to zero, but are less regular and oscillate around zero for the F-SpG (indicating a lack of clear plateau and upward/downward drifts in the SUP-G sensor response (figure 5(b))). However, mathematical modelling of chemical kinetics and rate of adsorption of gas molecules can precisely be described using modified Langmuir adsorption model [74].

The response for both sensors is linear only for the first steps (0 to ∼800 ppm) in gas concentration and it then becomes non-linear as the response saturates at HCHO concentration ⩾800 ppm and ⩾1000 ppm for F-SGAS and F-SpG respectively. As per the density functional theory calculations, done by Wang *et al*, the adsorption of an HCHO molecule donates 0.021–0.039 electrons to single wall CNT [75]. A clear step response can be seen for F-SGAS before the saturation point, whereas the rate of adsorption at higher concentrations for SpG sensor is hindered. The saturation of response for both could be attributed due to the maximum possible number of active sites i.e. OH groups of TFQ on graphene for the given TFQ concentration (3% in acetone) used in this study. The F-SGAS's response appears to be perfectly expressed by a sigmoid function of the gas concentration x, scaled by 0.5: $S(x) = (1 + e^{-x})^{-1} - 0.5$ but this is not the case for the F-SpG. A sigmoid response is the result of a linear response at lower concentrations and saturation at higher concentrations, which is not unusual and often seen in the case of gas sensor [76]. While a linear behaviour would be ideal for any sensor, a non-linear, sigmoid response is still a predictable behaviour that can be used to calibrate a sensor's output in terms of gas concentrations.

A reversible sensor response is critical to its use in real-time gas sensing, and the greater the rate of forward and reverse response the wider the range of practical applications for the sensor. The desorption that allows the graphene sensor response to reverse or reset is typically very slow and it is therefore extremely important, for practical applications, to enhance the desorption [59, 77]. To accelerate the desorption of formaldehyde, the direct substrate heating was discarded to avoid the damage of SUS-G membranes (discussed earlier) and TFQ coating. Also, no reports exist for a UV-assisted gas desorption from a functionalized graphene surface. However, UV aided desorption from pristine graphene and CNTs surface has been reported [78, 79]. We, therefore, for the first time, adopted low energy UV irradiation to accelerate the formaldehyde desorption from the surface of TFQ modified F-SGAS/F-SpG chip. The efficacy of UV in accelerating the desorption of HCHO was tested by exposing the devices to a UV LED, mounted in close proximity (∼2 cm), powered at ∼200 mW at 6.5 V. The experimental

cycle, during which the sensor response was continuously recorded (figures 5(c) and (d)), consisted of injection into the chamber of sufficient HCHO to eventually mix to a selected concentration (in total three cycles of 400, 500, 800 ppm for F-SGAS and 200 ppm only for F-SpG), subsequent to the establishment of this concentration the chamber was vented eventually decreasing the concentration to zero. The HCHO concentration was therefore likely to be continually but predictably variable between 0 and the target concentration. Both the modelled concentration profile (green line) and, the period between injection and the start of venting (red rectangle) are shown for the experiments with F-SGAS/F-SpG (figures 5(c) and (d)).

Firstly, a comparison of F-SGAS's response to the modelled HCHO concentration shows that the sensor responds rapidly to the increase in concentration and slowly to the decrease in concentration—presumably due to the slow desorption, which is accelerated by the UV illumination (figure 5(c), F-SGAS response (black), idealized (red) and presumed (green) HCHO concentration profile). By extrapolating the unaided decay profile (blue dotted line) in desorption, it is possible to calculate that the level of UV illumination used decreases the recovery time by 15 m from 400 ppm and 5 m from 800 ppm. The reason for this enhancement is the subject of further study, although a weak and reversible electrostatic interaction between OH groups in TFQ and HCHO molecules has been proposed in literature [62]. It is worthwhile to note the actual UV energy impinging on graphene surface could not be calculated accurately for these experiments due to the lack of appropriate instrumentation. However, the UV illumination does not change the suspended structure in F-SGAS sensor and its subsequent capability of sensing is unaltered during progression through the three cycles of UV illumination (figure 5(c)). A potential reason for this could be that the impinged UV energy (36.12 kJ mol^{-1} (or ∼6 × 10^{-20} J), S5.3, SI) at the sensor might be sufficient enough to break HCHO–OH intermediate species (dissociation energy not known) but not between TFQ and graphene (π–π dissociation bond energy, ∼264 kJ mol^{-1} (or ∼44 × 10^{-20} J)) and C–C bonds (dissociation energy of 347 kJ mol^{-1} (∼58 × 10^{-20} J)) in graphene (S5.3, SI) [80, 81].

Secondly, F-SpG behaves quite differently compared to the F-SGAS (figure 5(d)). The response differs after each cycle—injection, exhaust, UV illumination—despite being challenged with an identical concentration (200 ppm) each time. The difference is largely a result of reduced baseline which drops by as much as 5% (∼12 mV). This is probably a result of water, oxygen and nitrogen molecules being trapped between graphene and the SiO$_2$ surface. Under UV irradiation, these can influence the conductivity of graphene [82, 83]. Water molecules and
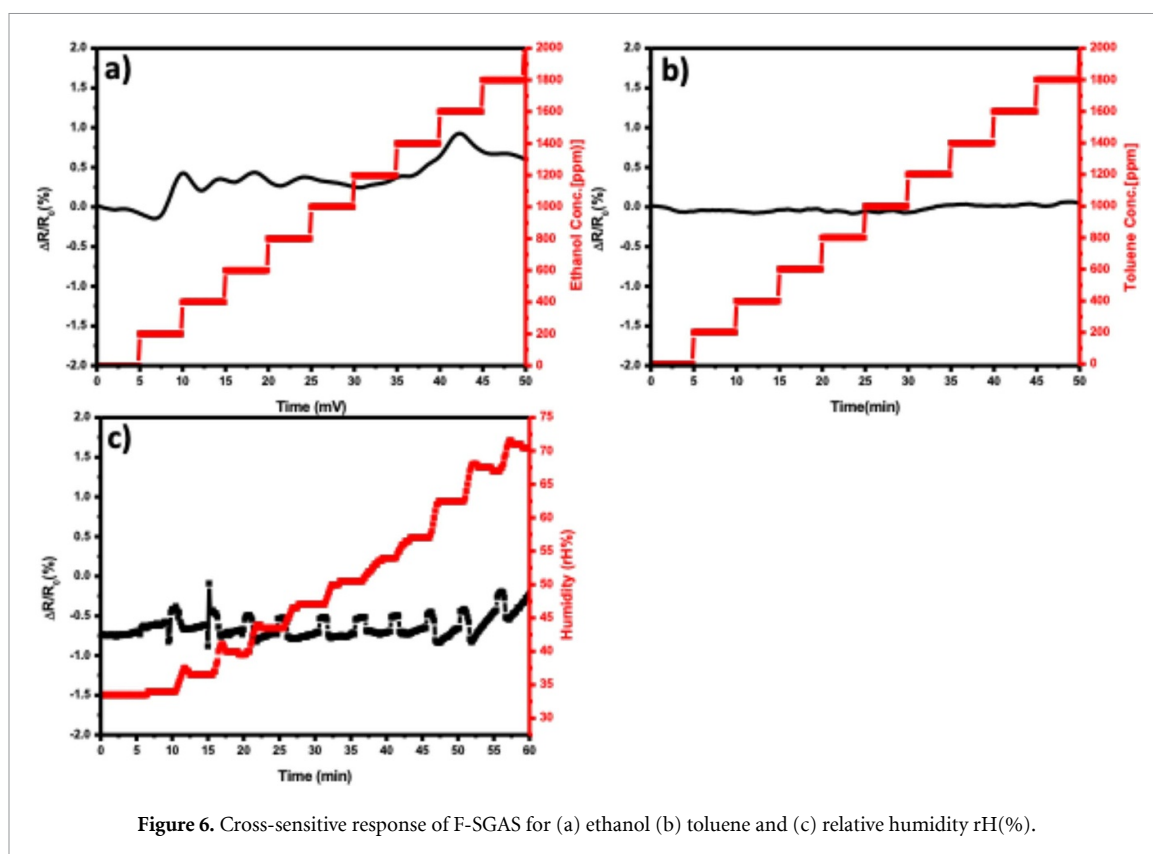
Figure 6. Cross-sensitive response of F-SGAS for (a) ethanol (b) toluene and (c) relative humidity rH(%).

silanol groups e.g. photodissociate into hydrogen radicals (H·), hydroxyl radicals (·OH) and radical (–Si·, Si−O·), which in turn react with the graphene lattice [84], changing the carbon orbitals from sp^2 to sp^3. This increases the electrical resistance, ultimately reducing the baseline voltage. It is also ascertained that (due to reduced charge trapping in SGAS) the effect of UV irradiation is significantly reduced for a F-SGAS chip compared to the F-SpG. It is, anticipated that with further optimization in chemical treatment and the power and exposure time of applied UV, an improvement in LOD can be achieved for selective real time HCHO monitoring within a complex gas environment.

The specificity of TFQ modified SUP-G device against acetone, ethanol and humidity has been reported by Tang *et al* [62], however, here we further validate this whilst exposing F-SGAS to two control gases (ethanol and toluene) at concentrations from 0 to 1800 ppm and relative humidity varying from ambient to 75% in the gas chamber. Figure 6 shows a panel of F-SGAS response plots obtained for varying concentrations of ethanol (figure 6(a)), toluene (figure 6(b)) and relative humidity (rH (%), figure 6(c)) in the glass chamber (figure S5.1, SI). The two solvents (ethanol and toluene) were chosen because bare graphene is known to be sensitive to both these control gases [33] and HCHO (figures S6.1 (b)–(d)), and also these control gases are likely to be present in industrial environments where HCHO is

typically produced. It is also worth mentioning that an unfunctionalized SpG sensor also shows sensitivity to HCHO (figure S6.1(d), SI), albeit with lower sensitivity compared to both F-SGAS and F-SpG. The concentration of both ethanol and toluene was systematically increased (manually by injecting in the 5 l chamber, in steps of 2.39 μl (200 ppm) of ethanol and 4.35 μl (200 ppm) toluene, shown as the red stepped function).

The injected quantity of solvent volatilizes at RT and atmospheric pressure. It is evident that the F-SGAS sensor does not respond to the control gases (figures 6(a) and (b)), which is in concurrence with work reported by Tang *et al* [62]. Besides, testing the specificity of F-SGAS chip for control gases, sensor response for increase in chamber relative humidity (rH%) was also investigated (figure 6(c)). Relative humidity of the glass chamber was elevated from ~32% (ambient) to 75%, whilst introducing water droplet of appropriate quantity into the chamber and evaporating it using a heat gun placed outside but near to the syringe injection point (figure S5.1(c), SI). A commercial humidity data logger (LASCAR Electronics, UK) was used to measure the chamber temperature and rH (%) in real time (figure S6.1(d), SI). From figure 6(c), it evident that F-SGAS does not responds to the increase in rH (%) as it responds to HCHO (figure 5(a)). The apparent no cross-sensitivity from control gases for F-SGAS could be due to the zero-binding affinity of ethanol

and toluene molecules with TFQ and thus no charge transfer to/from graphene. On the other hand, for the strong immunity to water molecules, we agree with the possible explanation proposed by Tang *et al* [62]. that the TFQ presence on graphene might avoid water molecules interaction resulting into no charge transfer to graphene, which is contrary to what is the case for a bare graphene device [85]. From figure 6(c). it can also be noted that the instant fluctuations in sensor response, at every instant of water injection, might be due to electrical disturbances (electrical humming) caused by the switching (power on/off) of the heat gun set-up in close proximity of glass (figure S5.1(c)). A small increase (<1%) in sensor response start appearing for rH (%) >∼65%, which could be to drifting of sensor response after running around one hour continuously. Figure S5.8 (SI) provides more evidence of specificity of a TFQ functionalized SGAS for HCHO when compared with bare SGAS response for these control gases.

2.3. Conclusions

The maintenance of the structural and electrical performance of graphene in an SGAS chip and its capability in gas sensing both to single gases and to a specific gas has been demonstrated. The chip is fully compatible with microelectronics fabrication standards, the sensor benefits from a highly parallel architecture consisting of 64 devices connected in parallel, each containing 180 individual portions of graphene suspended over cavities. A very high quality and yield (56%) of fully intact/SUS-G was obtained using the proposed GFS based graphene transfer. The GFS transfer method also ensures the standardize deposition of metal contact lines clamping graphene film on SiO_2/Si substrate—significant progress in standard step-wise microfabrication of SUS-G structures for micro electro mechanical system (MEMS) applications. From the electrical point of view, the main advantage of using SUS-G instead of SUP-G is that the final devices appear to have one order of magnitude lower overall electrical resistance, resulting in much more sensitive electrical readouts. This indicates a clear advantage of having an array of SUS-G membranes-based sensor configuration. From the gas sensing point of view, the use of SUS-G improves the sensitivity (responsivity) to NH_3, NO_2, and CO by an order of magnitude compared to SUP-G devices reported so far.

In terms of LOD, while the unfunctionalized devices can detect as low as ∼50 ppb NO_2, ∼108 ppb CO and ∼34 ppm N_3 in a controlled flow chamber and a TFQ functionalized sensor detect formaldehyde whilst showing no cross-sensitivity against the selective control gases; ethanol, toluene and humidity. Very importantly, an accelerated reset mechanism was demonstrated using UV irradiation from a low power light emitting diode without affecting the sensor sensitivity for formaldehyde and sever damage

to the SUS-G structure. Crucially, a device based on SUP-G appears to deteriorate under UV irradiation, with the baseline severely drifting by as much as ∼12 mV.

While some issues still require addressing, e.g. using higher crystalline quality graphene to increase yield and reproducibility, the chipset presented is already an advanced prototype specific formaldehyde sensor, with required sub-ppm LOD, minimal cross-sensitivity for more gases, mass producible, and furthermore resettable. This knowledge is critical to develop a route for the complete construction of an electronic nose (e-nose) for simultaneous detection of multiple target gases from a mixture. An e-nose could be constructed either by connecting multiple number of differently functionalized 3 mm × 3 mm SGAS chip-sets into a single package or by having different coatings on a 15 mm × 15 mm SGAS die. Thus, realizing such prototype demonstrates the potential for SUS-G to finally construct a 2D material-based e-nose system in the electronic market. This is something to achieve in future work.

3. Materials and methods

3.1. Fabrication of SGAS/SpG sensor chip

A brief account on the sensor fabrication steps (patent pending [39]) is given in this section, with more information given in section S1 of SI (supplementary information). The substrates used for this experiment were 15 mm × 15 mm Si (Si <100>, n+ type, 50 Ω cm^{-2}) die with ∼1.5 μm thick SiO_2 film grown through wet oxidation process (section S1, SI). Each substrate contains 16 number of SGAS chips arranged in 4 × 4 array configuration and each sensor chip contain 64 sensor devices. Individual sensor device consists of monolayer graphene film suspended over an array of 180 square cavities and connected by metal contacts at both the ends of cavities array as shown in figure 1(a). The fabrication process steps include three major steps;

(a) Pre-transfer device fabrication (substrate preparation and cavity array formation); multiple arrays of square (6 μm × 6 μm)/circular (6 μm, diameter) cavities were etched to a depth of ∼1 μm in (∼1.5 μm) thick SiO_2 layer of SiO_2/Si (<100>, n+ type, 50 Ω cm^{-2}) substrate die using RIE (section S1, figures S1.1(a)–(i) and S2(a)–(c)). The cavities were etched using RIE at an etch rate of ∼1.2 nm sec^{-1} to 1.3 nm sec^{-1} using a mixture of CHF_3 (25 sccm), Ar (25 sccm) at a chamber pressure of 30 mtorr, inductively coupled power of 160 W, radio frequency power of 160 W and DC bias of 622.

(b) GFS (Al/PPR/GR) preparation and wet transfer; a square piece (12 mm × 12 mm) of CVD monolayer graphene on 25 μm thick Cu film

(from 2D-tech, Manchester) was cut out and graphene on the top side was protected with a positive tone photoresist (PPR) (S1813, Shipley) followed by thermal deposition of ~50 nm Al (UV barrier) layer (section S1, figures S1.1(j)–(l)). Graphene on the back side of the Cu film was etched clean using O_2 plasma (and Cu film was removed whilst dissolving in 0.25 M ammonium persulphate solution. GFS was then transferred on O_2 plasma cleaned SiO_2/Si substrate (15 mm × 15 mm, die with cavities array) after thorough rinsing in Di-H_2O (section 1, figures S1.1(m) and S2(d)). After the GFS transfer, the substrate was spun at high speed (6 k rpm) to remove any water molecules trapped under the GFS. Lastly, the substrate was heated at 50 °C for 5 min to improve the adhesion of GFS (or graphene) with SiO_2.

(c) Post transfer fabrication (metal contacts deposition and CPD); GFS on SiO_2/Si substrate was lithographically patterned and Al/PPR layer was selectively removed (using wet etching) to open windows on graphene for Cr/Au contact lines (section 1, figures S1(n) and S1.2(e)–(h)), a 10 nm of Cr and 100 nm of Au films were then thermally deposited at very low vacuum (2×10^{-6} torr). Following which the Cr/Au metal film was lithographically patterned and wet chemically etched to obtain 100 μm wide contact lines connecting all devices in parallel, as shown in figure 1(b) (section S1, figures S1.1(p) and S1.2(i)). Following the metallization step, UV barrier Al layer was completely removed in Al etchant solution and the substrate was moved to a CPD chamber to dissolve the PPR protecting graphene film over the cavities with acetone (section 1, figures S1.1(q) and S1.2(j)). Thermal annealing (280 °C under N_2 environment for 10 min) and current induced annealing were also performed on the substrate, after the CPD step, to obtain a good metal contacts adhesion and removal of any polymeric residues. The substrate was then scribed and diced into 9 mm^2 chips (figure S1.2(k)) and wire bonded into DIL ceramic package sockets for electrical characterization and gas detection testing (figures S1.2(m)–(o)). For comparison, SUP-G sensor chipset, in which CVD graphene on SiO_2/Si substrate with no cavities array, was fabricated using the same methods (figures S1(r) and S1.2).

3.2. Instruments

SUS-G membranes in SGAS were characterized using SEM (Quanta 200/Zeiss Ultra, UK), AFM (Asylum, UK) and Raman spectrum (Renishaw InVia^{TM} confocal, UK) to evaluate the yield and quality of SUS-G membranes. Electrical characterization was performed using an Agilent Technologies E5270B

(UK) measurement mainframe fitted with four E5287A source measure units (SMUs), in which each SMU was connected with a Karl Suss-PH100 micromanipulator probe with tungsten tip. A brief account of the parametric conditions set for AFM, SEM, XPS, Raman spectrums and electrical measurements is given in section S2 (SI). High-resolution SEM images were collected under low vacuum 2×10^{-6} torr with electron beam energy (25 keV) and spot size of 3.0 nm. AFM height images, of $30\,\mu$m × $30\,\mu$m size, were collected at slow scan speed of ~10 μm s^{-1}, scan rate of 0.1 Hz and with line resolution of 256 × 256 lines. XPS spectra were collected using a SPECS Sage HR 100 spectrometer with a non-monochromatic x-ray source of aluminium with a Kα line of 1486.6 eV energy and 300 W. The Raman maps were recorded with a 532 nm wavelength laser, a lens-based spectrometer with 1200/1800 gr mm^{-1} grating and a Peltier-cooled front-illuminated CCD (1024 px × 532 px). The data were analysed using WIRE 4.4 software. Additional information on Raman spectrum data analysis for a chemically treated SGAS is given in detail in section S5.2 (SI).

3.3. Experiment setup for gas sensor

A gas flow mechanism was set-up for NH_3, NO_2 and CO and a gas diffusion mechanism was set-up for HCHO (37% in water, Sigma Aldrich) detection section S4 (SI). The sensor's response (V_{RL}) is measured across the load resistance R_L connected in series with R_S (total chip resistance) and $R_L = R_S = R_0$, where R_0 is the initial (or baseline) resistance at RT and atm. pressure, and the circuit was supplied with a 1 V DC voltage (Keysight, PS, E36311A, UK) (figure 3(a)). A 4-channel Analog Data Logger (HOBO from ONSET, UK) was used to record the temporal variation of V_{RL} when exposed to the increasing concentration of tested gases. For the chemical treatment, SGAS chips were immersed in a ~5 ml of solution made of 0.3%wt of TFQ (96%, Alfa Aesar) in acetone (95%, Sigma Aldrich) for 30 min followed by drying under ambient conditions. SEM, XPS and RM/RS data was collected before and after the chemical treatment. UV assisted SGAS recovery (or sensor resetting) of the HCHO gas (distortion) was achieved by powering a UV LED (UV5TZ-390-30 Bivar, UV LED, 390 nm, 40 mW, 30 °C, 2-pin, RS components, UK) at ~100 mW @ 6.5 V.

and advise on CVD graphene and scale-up, University of Manchester, United Kingdom and the Maria de Maeztu Units of Excellence Program from the Spanish State Research, Agency (Grant No. MDM-2017-0720). RKG and MM are also thankful to Dr. Meyya Meyyappan, NASA Ames Research Center, California, USA for his very insightful discussion and advice whilst preparing the manuscript

Conflict of interest

The authors declare no competing financial interest.

ORCID iDs

Rakesh K Gupta ⦿ https://orcid.org/0000-0001-9396-2556

Omar M Dawood ⦿ https://orcid.org/0000-0003-3655-0656

Alejandro Criado ⦿ https://orcid.org/0000-0002-9732-513X

Caroline Dang ⦿ https://orcid.org/0000-0001-9178-9286

Robert J Young ⦿ https://orcid.org/0000-0001-6073-9489

Leszek Majewski ⦿ https://orcid.org/0000-0001-6544-1286

Max A Migliorato ⦿ https://orcid.org/0000-0001-8394-7854

References

[1] Capone S *et al* 2003 Solid state gas sensors: state the art and future activities *J. Optoelectron. Adv. Mater.* **5** 1335–48

[2] Dutta P and Horn P 1981 Low-frequency fluctuations in solids: 1 f noise *Rev. Mod. Phys.* **53** 497

[3] Wang C, Yin L, Zhang L, Xiang D and Gao R 2010 Metal oxide gas sensors: sensitivity and influencing factors *Sensors* **10** 2088–106

[4] Ponzoni A, Baratto C, Cattabiani N, Falasconi M, Galstyan V, Nunez-Carmona E, Rigoni F, Sberveglieri V, Zambotti G and Zappa D 2017 Metal oxide gas sensors, a survey of selectivity issues addressed at the SENSOR Lab, Brescia (Italy) *Sensors* **17** 714

[5] Hunter G W *et al* 2020 Editors' choice—critical review—a critical review of solid state gas sensors *J. Electrochem. Soc.* **167** 037570

[6] Das S and Jayaraman V 2014 SnO2: a comprehensive review on structures and gas sensors *Prog. Mater. Sci.* **66** 112–255

[7] Dey A 2018 Semiconductor metal oxide gas sensors: a review *Mater. Sci. Eng.* B **229** 206–17

[8] Goldoni A 2014 Nanostructured carbon-based materials for gas sensor applications: *2014 Aeit Annual Conf.—from Research to Industry: The Need for a More Effective Technology Transfer (Aeit)* (https://doi.org/10.1109/AEIT.2014.7002033)

[9] Park S J, Park C S and Yoon H 2017 Chemo-electrical gas sensors based on conducting polymer hybrids *Polymers* **9** 155

[10] Chatterjee S G, Chatterjee S, Ray A K and Chakraborty A K 2015 Graphene–metal oxide nanohybrids for toxic gas sensor: a review *Sensors Actuators* B **221** 1170–81

[11] Zeng W N *et al* 2009 Progress in conjugated polymer sensors for detecting pathogens *Chin. J. Org. Chem.* **29** 1858–66 (https://www.researchgate.net/publication/286396884_Progress_in_Conjugated_Polymer_Sensors_for_Detecting_Pathogens)

[12] Bag A and Lee N-E 2019 Gas sensing with heterostructures based on two-dimensional nanostructured materials: a review *J. Mater. Chem.* C **7** 13367–83

[13] Meyyappan M 2016 Carbon nanotube-based chemical sensors *Small* **12** 2118–29

[14] Buckley D, Black N C G, Castanon E G, Melios C, Hardman M and Kazakova O 2020 Frontiers of graphene and 2D material-based gas sensors for environmental monitoring *2D Mater.* **7** 3

[15] Wang T *et al* 2016 A review on graphene-based gas/vapor sensors with unique properties and potential applications *Nano-Micro Lett.* **8** 95–119

[16] Meng Z, Stolz R M, Mendecki L and Mirica K A 2019 Electrically-transduced chemical sensors based on two-dimensional nanomaterials *Chem. Rev.* **119** 478–598

[17] Jing Z, Guang-Yu Z and Dong-Xia S 2013 Review of graphene-based strain sensors *Chin. Phys.* B **22** 057701

[18] Tang Y C, Zhao Z, Hu H, Liu Y, Wang X, Zhou S and Qiu J 2015 Highly stretchable and ultrasensitive strain sensor based on reduced graphene oxide microtubes-elastomer composite *ACS Appl. Mater. Interfaces* **7** 27432–9

[19] Novoselov K S, Geim A K, Morozov S V, Jiang D, Katsnelson M I, Grigorieva I V, Dubonos S V and Firsov A A 2005 Two-dimensional gas of massless Dirac fermions in graphene *Nature* **438** 197–200

[20] Liu Y, Dong X and Chen P 2012 Biological and chemical sensors based on graphene materials *Chem. Soc. Rev.* **41** 2283–307

[21] Jiang H 2011 Chemical preparation of graphene-based nanomaterials and their applications in chemical and biological sensors *Small* **7** 2413–27

[22] Sun J, Muruganathan M and Mizuta H 2016 Room temperature detection of individual molecular physisorption using suspended bilayer graphene *Sci. Adv.* **2** 1–7

[23] Chen G, Paronyan T M and Harutyunyan A R 2012 Sub-ppt gas detection with pristine graphene *Appl. Phys. Lett.* **101** 053119

[24] Schedin F *et al* 2007 Detection of individual gas molecules adsorbed on graphene *Nat Mater* **6** 652–5

[25] Pirkle A, Chan J, Venugopal A, Hinojos D, Magnuson C W, McDonnell S, Colombo L, Vogel E M, Ruoff R S and Wallace R M 2011 The effect of chemical residues on the physical and electrical properties of chemical vapor deposited graphene transferred to SiO2 *Appl. Phys. Lett.* **99** 122108

[26] Lau C N, Bao W and Velasco J 2012 Properties of suspended graphene membranes *Mater. Today* **15** 238–45

[27] Gao L, Ni G-X, Liu Y, Liu B, Castro Neto A H and Loh K P 2014 Face-to-face transfer of wafer-scale graphene films *Nature* **505** 190

[28] Liang X L *et al* 2011 Toward clean and crackless transfer of graphene *Acs Nano* **5** 9144–53

[29] Chen Y, Gong X L and Gai J G 2016 Progress and challenges in transfer of large-area graphene films *Adv. Sci.* **3** 1500343

[30] Georgakilas V, Otyepka M, Bourlinos A B, Chandra V, Kim N, Kemp K C, Hobza P, Zboril R and Kim K S 2012 Functionalization of graphene: covalent and non-covalent approaches, derivatives and applications *Chem. Rev.* **112** 6156–214

[31] Sreeprasad T and Berry V 2013 How do the electrical properties of graphene change with its functionalization? *Small* **9** 341–50

[32] Kim B, Norman T J, Jones R S, Moon D-I, Han J-W and Meyyappan M 2019 Carboxylated single-walled carbon nanotube sensors with varying pH for the detection of ammonia and carbon dioxide using an artificial neural network *ACS Appl. Nano Mater.* **2** 6445–51

[33] Rumyantsev S, Liu G, Shur M S, Potyrailo R A and Balandin A A 2012 Selective gas sensing with a single pristine graphene transistor *Nano Lett.* **12** 2294–8

[34] Wiederoder M S, Nallon E C, Weiss M, McGraw S K, Schnee V P, Bright C J, Polcha M P, Paffenroth R and Uzarski J R 2017 Graphene nanoplatelet-polymer chemiresistive

sensor arrays for the detection and discrimination of chemical warfare agent simulants *ACS Sens.* **2** 1669–78

[35] Bolotin K I, Sikes K J, Jiang Z, Klima M, Fudenberg G, Hone J, Kim P and Stormer H L 2008 Ultrahigh electron mobility in suspended graphene *Solid State Commun.* **146** 351–5

[36] Aleman B *et al* 2010 Transfer-free batch fabrication of large-area suspended graphene membranes *ACS Nano* **4** 4762–8

[37] Monteverde U, Pal J, Migliorato M A, Missous M, Bangert U, Zan R, Kashtiban R and Powell D 2015 Under pressure: control of strain, phonons and bandgap opening in rippled graphene *Carbon* **91** 266–74

[38] Cheng Z, Li Q, Li Z, Zhou Q and Fang Y 2010 Suspended graphene sensors with improved signal and reduced noise *Nano Lett.* **10** 1864–8

[39] Migliorato Max*et al* 2019 Methods of manufacturing a graphene-based device 2574412A UK (https://patents.google.com/patent/GB2574412A)

[40] Wagner S *et al* 2016 Graphene transfer methods for the fabrication of membrane-based NEMS devices *Microelectron. Eng.* **159** 108–13

[41] Chen Y-M *et al* 2016 Ultra-large suspended graphene as highly elastic membrane for capacitive pressure sensor *Nanoscale* **8** 3555–64

[42] Gajewski K, Goniszewski S, Szumska A, Moczała M, Kunicki P, Gallop J, Klein N, Hao L and Gotszalk T 2016 Raman spectroscopy and kelvin probe force microscopy characteristics of the CVD suspended graphene *Diam. Relat. Mater.* **64** 27–33

[43] Dawood O M, Gupta R K, Monteverde U, Alqahtani F H, Kim H-Y, Sexton J, Young R J, Missous M and Migliorato M A 2019 Dynamic modulation of the Fermi energy in suspended graphene backgated devices *Sci. Technol. Adv. Mater.* **20** 568–79

[44] Ovid'Ko I 2013 Mechanical properties of graphene *Rev. Adv. Mater. Sci* **34** 1–11 (http://www.ipme.ru/e-journals/RAMS/no_13413/01_13413_ovidko.pdf)

[45] Wang X, Tian H, Xie W, Shu Y, Mi W-T, Ali Mohammad M, Xie Q-Y, Yang Y, Xu J-B and Ren T-L 2015 Observation of a giant two-dimensional band-piezoelectric effect on biaxial-strained graphene *NPG Asia Mater.* **7** e154

[46] Patil V, Capone A, Strauf S and Yang E-H 2013 Improved photoresponse with enhanced photoelectric contribution in fully suspended graphene photodetectors *Sci. Rep.* **3** 2791

[47] Ferrari A C and Basko D M 2013 Raman spectroscopy as a versatile tool for studying the properties of graphene *Nat Nanotechnol* **8** 235–46

[48] Jang S K, Jeon J, Jeon S M, Song Y J and Lee S 2015 Effects of dielectric material properties on graphene transistor performance *Solid State Electron.* **109** 8–11

[49] Kim J H, Zhou Q and Chang J Y 2017 Suspended graphene-based gas sensor with 1-mW energy consumption *Micromachines* **8**

[50] Yuan W J and Shi G Q 2013 Graphene-based gas sensors *J. Mater. Chem.* A **1** 10078–91

[51] Yavari F, Castillo E, Gullapalli H, Ajayan P M and Koratkar N 2012 High sensitivity detection of NO2 and NH3 in air using chemical vapor deposition grown graphene *Appl. Phys. Lett.* **100** 203120

[52] Gierz I, Riedl C, Starke U, Ast C R and Kern K 2008 Atomic hole doping of graphene *Nano Lett.* **8** 4603–7

[53] Varghese S S, Lonkar S, Singh K K, Swaminathan S and Abdala A 2015 Recent advances in graphene based gas sensors *Sensors Actuators* B **218** 160–83

[54] Joshi R K, Gomez H, Alvi F and Kumar A 2010 Graphene films and ribbons for sensing of O2, and 100 ppm of CO and NO2 in practical conditions *J. Phys. Chem.* C **114** 6610–3

[55] Ren Y, Chen S, Cai W, Zhu Y, Zhu C and Ruoff R S 2010 Controlling the electrical transport properties of graphene by in situ metal deposition *Appl. Phys. Lett.* **97** 053107

[56] Yoon H J, Jun D H, Yang J H, Zhou Z, Yang S S and Cheng M M-C 2011 Carbon dioxide gas sensor using a graphene sheet *Sensors Actuators* B **157** 310–3

[57] Smith A D *et al* 2013 Electromechanical piezoresistive sensing in suspended graphene membranes *Nano Lett.* **13** 3237–42

[58] Costa S, Weis J E, Frank O, Fridrichová M and Kalbac M 2016 Monitoring the doping of graphene on SiO 2/Si substrates during the thermal annealing process *RSC Adv.* **6** 72859–64

[59] Mortazavi Zanjani S M, Sadeghi M M, Holt M, Chowdhury S F, Tao L and Akinwande D 2016 Enhanced sensitivity of graphene ammonia gas sensors using molecular doping *Appl. Phys. Lett.* **108** 033106

[60] Han T H, Huang Y-K, Tan A T L, Dravid V P and Huang J 2011 Steam etched porous graphene oxide network for chemical sensing *J. Am. Chem. Soc.* **133** 15264–7

[61] Smith A D *et al* 2017 Graphene-based CO 2 sensing and its cross-sensitivity with humidity *RSC Adv.* **7** 22329–39

[62] Tang X, Mager N, Vanhorenbeke B, Hermans S and Raskin J-P 2017 Defect-free functionalized graphene sensor for formaldehyde detection *Nanotechnology* **28** 055501

[63] Lipatov A, Varezhnikov A, Wilson P, Sysoev V, Kolmakov A and Sinitskii A 2013 Highly selective gas sensor arrays based on thermally reduced graphene oxide *Nanoscale* **5** 5426–34

[64] Nomani M W, Shishir R, Qazi M, Diwan D, Shields V B, Spencer M G, Tompa G S, Sbrockey N M and Koley G 2010 Highly sensitive and selective detection of NO2 using epitaxial graphene on 6H-SiC *Sensors Actuators* B **150** 301–7

[65] Wu J-B *et al* 2018 Raman spectroscopy of graphene-based materials and its applications in related devices *Chem. Soc. Rev.* **47** 1822–73

[66] Lee J E, Ahn G, Shim J, Lee Y S and Ryu S 2012 Optical separation of mechanical strain from charge doping in graphene *Nat. Commun.* **3** 1–8

[67] Cheng Z, Zhou Q, Wang C, Li Q, Wang C and Fang Y 2011 Toward intrinsic graphene surfaces: a systematic study on thermal annealing and wet-chemical treatment of SiO2-supported graphene devices *Nano Lett.* **11** 767–71

[68] Lee J E, Ahn G, Shim J, Lee Y S and Ryu S 2012 Optical separation of mechanical strain from charge doping in graphene *Nat. Commun.* **3** 1024

[69] Dan Y, Lu Y, Kybert N J, Luo Z and Johnson A T C 2009 Intrinsic response of graphene vapor sensors *Nano Lett.* **9** 1472–5

[70] Liao C D, Lu Y-Y, Tamalampudi S R, Cheng H-C and Chen Y-T 2013 Chemical vapor deposition synthesis and Raman spectroscopic characterization of large-area graphene sheets *J. Phys. Chem.* A **117** 9454–61

[71] Ni Z H, Yu T, Lu Y H, Wang Y Y, Feng Y P and Shen Z X 2008 Uniaxial strain on graphene: Raman spectroscopy study and band-gap opening *ACS Nano* **2** 2301–5

[72] Sheet O F 2011 *Formaldehyde* (Washington, DC: The US Department of Labor)

[73] Lu Y, Meyyappan M and Li J 2010 A carbon-nanotube-based sensor array for formaldehyde detection *Nanotechnology* **22** 055502

[74] Black N, Rungger I, Li B, Maier S A, Cohen L F, Gallop J C and Hao L 2018 Adsorption dynamics of CVD graphene investigated by a contactless microwave method *2D Mater.* **5** 035024

[75] Wang R *et al* 2006 Boron-doped carbon nanotubes serving as a novel chemical sensor for formaldehyde *J. Phys. Chem.* B **110** 18267–71

[76] Gerasimov G 2017 Graphene-based gas sensors *Adv. Environ. Anal. Appl. Nanomater. Vol 2* **10** 133–52

[77] Ko G, Kim H-Y, Ahn J, Park Y-M, Lee K-Y and Kim J 2010 Graphene-based nitrogen dioxide gas sensors *Curr. Appl. Phys.* **10** 1002–4

[78] Sun P, Zhu M, Wang K, Zhong M, Wei J, Wu D, Cheng Y and Zhu H 2012 Photoinduced molecular desorption from graphene films *Appl. Phys. Lett.* **101** 053107

[79] Chen G, Paronyan T M, Pigos E M and Harutyunyan A R 2012 Enhanced gas sensing in pristine carbon nanotubes under continuous ultraviolet light illumination *Sci. Rep.* **2** 1–7

[80] Luo Y-R 2007 *Comprehensive Handbook of Chemical Bond Energies* (Boca Raton, FL: CRC press)

[81] Darwent B D 1970 *Bond Dissociation Energies in Simple Molecules* (Washington D.C.: National Standard Reference Data System)

[82] Ryu S, Liu L, Berciaud S, Yu Y-J, Liu H, Kim P, Flynn G W and Brus L E 2010 Atmospheric oxygen binding and hole doping in deformed graphene on a SiO2 substrate *Nano Lett.* **10** 4944–51

[83] Zhang E, Newaz A K M, Wang B, Zhang C X, Fleetwood D M, Bolotin K I, Schrimpf R D, Pantelides S T and Alles M L 2012 Ozone-exposure and annealing effects on graphene-on-SiO2 transistors *Appl. Phys. Lett.* **101** 121601

[84] Imamura G and Saiki K 2015 Modification of graphene/SiO2 interface by UV-irradiation: effect on electrical characteristics *ACS Appl. Mater. Interfaces* **7** 2439–43

[85] Smith A D *et al* 2015 Resistive graphene humidity sensors with rapid and direct electrical readout *Nanoscale* **7** 19099–109